

DiffComplete: Diffusion-based Generative 3D Shape Completion

Ruihang Chu¹ Enze Xie² Shentong Mo³
 Zhenguo Li² Matthias Nießner⁴ Chi-Wing Fu¹ Jiaya Jia¹
¹CUHK ²Huawei Noah's Ark Lab ³MBZUAI ⁴TUM
<https://ruihangchu.com/diffcomplete.html>

Abstract

We introduce a new diffusion-based approach for shape completion on 3D range scans. Compared with prior deterministic and probabilistic methods, we strike a balance between realism, multi-modality, and high fidelity. We propose DiffComplete by casting shape completion as a generative task conditioned on the incomplete shape. Our key designs are two-fold. First, we devise a hierarchical feature aggregation mechanism to inject conditional features in a spatially-consistent manner. So, we can capture both local details and broader contexts of the conditional inputs to control the shape completion. Second, we propose an occupancy-aware fusion strategy in our model to enable the completion of multiple partial shapes and introduce higher flexibility on the input conditions. DiffComplete sets a new SOTA performance (*e.g.*, 40% decrease on l_1 error) on two large-scale 3D shape completion benchmarks. Our completed shapes not only have a realistic outlook compared with the deterministic methods but also exhibit high similarity to the ground truths compared with the probabilistic alternatives. Further, DiffComplete has strong generalizability on objects of entirely unseen classes for both synthetic and real data, eliminating the need for model re-training in various applications.



Figure 1: Our method is able to (a) produce realistic completed shapes from partial scans, (b) incorporate multiple incomplete scans (denoted by the plus symbol) to improve the completion accuracy, and (c) directly generalize to work on real objects of unseen classes without finetuning.

1 Introduction

The advent of affordable range sensors, such as the Microsoft Kinect and Intel RealSense, has spurred remarkable progress in 3D reconstruction [1], facilitating applications in content creation, mixed reality, robot navigation, and more. Despite the improved reconstruction quality [2–5], typical scanning sessions cannot cover every aspect of the scene objects. Hence, the reconstructed 3D models often have incomplete geometry, thereby limiting their practical usage in downstream applications. To fully unlock the potential of 3D reconstruction for supporting assorted applications, it is essential to address the challenges of completing incomplete shapes.

Effectively, a shape completion should produce shapes that are *realistic*, *probabilistic*, and *high-fidelity*. First, the produced shapes should look plausible without visual artifacts. Second, considering the under-determined nature of completion, it is desirable for the model to generate diverse, multi-modal outputs when filling in the missing regions, to improve the likelihood of obtaining a superior shape and enable creative use. Third, while multiple outputs encourage the model’s generative ability, maintaining effective control over the completion results is crucial to ensure coherent reconstructions that closely resemble the ground-truth shapes.

Current approaches to 3D shape completion fall into deterministic and probabilistic paradigms. The former class excels at aligning predictions with ground truths, owing to their determined mapping functions and full supervision. However, this can expose the models to a higher risk of over-fitting, leading to undesirable artifacts, such as rugged surfaces, especially on unseen objects. On the other hand, probabilistic approaches formulate the shape completion as a conditional generation task to produce plausible results, paired with techniques like auto-encoding [6], adversarial training [7–9], or diffusion models [10–13]. These approaches mainly focus on cases that prioritize completion diversity, for instance, filling in large missing regions cropped out by 3D boxes, where the algorithm has more freedom to explore various plausible shapes. However, when completing shapes obtained from range scans/reconstructions, whose geometries are often contaminated with noise, having varying degrees of incompleteness (see row 1 in Fig. 1), the goal is to recover the ground-truth scanned objects as accurately as possible. Therefore, relying solely on previous probabilistic approaches may compromise the completion accuracy and leads to low-fidelity results.

In this work, we focus on completing shapes acquired from range scans, aiming to produce *realistic* and *high-fidelity* completed shapes, while considering also the *probabilistic* uncertainty. We approach this task as a conditional generation with the proposed diffusion model named DiffComplete. To address the accuracy challenge typically in probabilistic models, we introduce a key design that incorporates range scan features in a hierarchical and spatially-consistent manner to facilitate effective controls. Additionally, we propose a novel occupancy-aware fusion strategy that allows taking multiple partial shapes as input for more precise completions.

Specifically, we formulate the diffusion process on a truncated distance field in a volumetric space. This representation allows us to encode both complete and incomplete shapes into multi-resolution structured feature volumes, thereby enabling their interactions at various network levels. At each level, features are aggregated based on voxel-to-voxel correspondence, enabling precise correlation of the difference in partialness between the shapes. By leveraging multi-level aggregation, the completion process can be controlled by both local details and broader contexts of the conditional inputs to improve the completion accuracy and network generalizability, as shown in Sec. 4.5.

To condition the completion on multiple partial shapes, our occupancy-aware fusion strategy adopts the occupancy mask as a weight to adaptively fuse all observed geometry features from various incomplete shapes, and then employ the fused features to control the completion process. For robustness, such an operation is performed in a multi-scale feature space. With our novel design, switching between single and multiple conditions can be efficiently achieved by finetuning an MLP layer. As Fig. 1(b) and 6 show, using multiple conditions for completion progressively refines the final shapes towards the ground truths.

DiffComplete sets a new state-of-the-art performance on two large-scale shape completion benchmarks [14, 15] in terms of completion accuracy and visual quality. Compared to prior deterministic and probabilistic approaches, we not only generate multimodal plausible shapes with minimal artifacts but also present high shape fidelity relative to the ground truths. Further, DiffComplete can directly generalize to work on unseen object categories. Without specific zero-shot designs, it surpasses all existing approaches for both synthetic and real-world data, allowing us to eliminate the need for model re-training in various applications. To sum up, our contributions are listed as follows:

- We introduce a diffusion model to complete 3D shapes on range scans, enabling realistic, probabilistic, and high-fidelity 3D geometry.
- To improve the completion accuracy, we enable effective control from single-input condition by hierarchical and spatially-consistent feature aggregation, and from multiple ones by an occupancy-aware fusion strategy.
- We show SOTA performance on shape completion on both novel instances and entirely unseen object categories, along with an in-depth analysis on a range of model characteristics.

2 Related Work

RGB-D reconstruction. Traditional methods rely on geometric approaches for 3D reconstruction [16–20]. A pioneering method [21] proposes a volumetric fusion strategy to integrate multiple range images into a unified 3D model on truncated signed distance fields (TSDF), forming the basis for many modern techniques like KinectFusion [22, 23], VoxelHashing [24], and BundleFusion [2]. Recent learning-based approaches further improve the reconstruction quality with fewer artifacts [25–28, 3], yet the intrinsic occlusions and measurement noise of 3D scans constrain the completeness of 3D reconstructions, making them still less refined than manually-created assets.

3D shape completion is a common post-processing step to fill in missing parts in the reconstructed shapes. Classic methods mainly handle small holes and geometry primitives via Laplacian hole filling [29–31] or Poisson surface reconstruction [32, 33]. Another line exploits the structural regularities of 3D shapes, such as the symmetries, to predict the unobserved data [34–38].

The availability of large 3D data has sparked retrieval-based methods [39–42] and learning-based fitting methods [43, 44, 14, 45–49]. The former retrieves the shapes from a database that best match the incomplete inputs, whereas the latter minimizes the difference between the network-predicted shapes and ground truths. 3D-EPN [14], for instance, proposes a 3D encoder-decoder architecture to predict the complete shape from partial volumetric data. Scan2Mesh [50] converts range scans into 3D meshes with a direct optimization on the mesh surface. PatchComplete [15] further leverages local structural priors for completing shapes of unseen categories.

Generative methods, e.g., GANs [51, 9, 52, 7, 8] and AutoEncoders [6, 53], offer an alternative to shape completion. Being able to generate diverse plausible global shapes based on a partial input, they allow for high generation freedom and thus compromise the completion accuracy in scenarios where a ground truth exists [51]. Distinctively, we employ a powerful diffusion model for shape completion, specifically designed to prioritize the fidelity relative to ground truths while retaining the output diversity. Compared to both generative and fitting-based paradigms, our method also effectively reduces surface artifacts, producing more realistic and natural 3D shapes. In addition, we show superior generalization ability on completing objects of novel classes over SOTAs.

Diffusion models for 3D generation. Diffusion models [54–61] have shown superior performance in various generation tasks, outperforming GANs’ sample quality while preserving the likelihood evaluation property of VAEs. When adopted in 3D domain, a range of works [12, 62–64] focus on point cloud generation. For more complex surface generation, some works [65, 13, 10, 66, 67, 11] adopt latent diffusion models to learn implicit neural representations and form final shapes via a decoder. While some others [10–13] support conditional shape completion, they typically fill in large regions cropped out with 3D boxes or reconstruct reasonable shapes from images. Due to the absence of meaningful ground truths in these completion scenarios, they could also face completion accuracy challenges like the above generative approaches [51, 9, 52, 7, 8]. Instead, our method concentrates on completing shapes acquired from range scans, yielding outputs closely resembling the actual objects scanned. Also, we apply the diffusion process in explicit volumetric TSDFs, preserving more geometrical structures during the completion process.

3 Method

3.1 Formulation

To prepare the training data, we generate an incomplete 3D scan from depth frames using volumetric fusion [21] and represent the scan as a truncated signed distance field (TSDF) in a volumetric grid. Yet, to accurately represent a ground-truth shape, we choose to use a volumetric truncated unsigned distance field (TUDF) instead. This is because retrieving the sign bit from arbitrary 3D CAD models (e.g., some are not closed) is non-trivial. By using TUDF, we can robustly capture the geometric features of different objects without being limited by the topology.

Given such a volume pair, *i.e.*, the incomplete scan c and complete 3D shape x_0 , we formulate the shape completion as a generation task that produces x_0 conditioned on c . We employ the probabilistic diffusion model as our generative model. In particular, it contains (i) a *forward process* (denoted as $q(x_{0:T})$) that gradually adds Gaussian noise to corrupt the ground-truth shape x_0 into a random noise volume x_T , where T is the total number of time steps; and (ii) a *backward process* that employs

a shape completion network, with learned parameters θ , to iteratively remove the noise from x_T conditioned on the partial scan c and produce the final shape, denoted as $p_\theta(x_{0:T}, c)$. As both the *forward* and *backward* processes are governed by a discrete-time Markov chain with time steps $\{0, \dots, T\}$, their Gaussian transition probabilities can be formulated as

$$q(x_{0:T}) = q(x_0) \prod_{t=1}^T q(x_t|x_{t-1}), \quad q(x_t|x_{t-1}) := \mathcal{N}(\sqrt{1 - \beta_t}x_{t-1}, \beta_t \mathbf{I}) \quad (1)$$

$$\text{and } p_\theta(x_{0:T}, c) = p(x_T) \prod_{t=1}^T p_\theta(x_{t-1}|x_t, c), \quad p_\theta(x_{t-1}|x_t) := \mathcal{N}(\mu_\theta(x_t, t, c), \sigma_t^2 \mathbf{I}). \quad (2)$$

In the *forward* process (Eq. (1)), the scalars $\beta_t \in [0, 1]$ control a variance schedule that defines the amount of noise added in each step t . In the *backward* process (Eq. (2)), $p(x_T)$ is a Gaussian prior in time step T , μ_θ represents the mean predicted from our network and σ_t^2 is the variance. As suggested in DDPM [59], predicting $\mu_\theta(x_t, t, c)$ can be simplified to alternatively predicting $\epsilon_\theta(x_t, t, c)$, which should approximate the noise used to corrupt x_{t-1} in the *forward* process, and σ_t can be replaced by the pre-defined β_t . With these modifications, we can optimize the network parameter θ with a mean squared error loss to maximize the generation probability $p_\theta(x_0)$. The training objective is

$$\arg \min_{\theta} E_{t, x_0, \epsilon, c} [\|\epsilon - \epsilon_\theta(x_t, t, c)\|^2], \quad \epsilon \in \mathcal{N}(0, \mathbf{I}) \quad (3)$$

where ϵ is the applied noise to corrupt x_0 into x_t and $\mathcal{N}(0, \mathbf{I})$ denotes a unit Gaussian distribution. We define all the diffusion processes in a volume space of a resolution S^3 , i.e., $x_{0:T}, c, \epsilon \in \mathbb{R}^{S \times S \times S}$, where each voxel stores a scalar TSDF/TUFD value; $S=32$ in our experiments. Compared to previous latent diffusion models [11, 13, 65, 10] that require shape embedding first, we directly manipulate the shape with a better preservation of geometric features. Doing so naturally enables our hierarchical feature aggregation strategy (see Sec. 3.2). Next, we will introduce how to predict $\epsilon_\theta(x_t, t, c)$.

3.2 Shape Completion Pipeline

Overview. To enhance the completion accuracy, we encourage the incomplete scans to control completion behaviors. Inspired from the recent ControlNet [68], which shows great control ability given 2D conditions, we adopt a similar principle to train an additional control branch. To predict the noise $\epsilon_\theta(x_t, t, c)$ in Eq. (3), we encode the corrupted ground-truth shape x_t by a main branch and the partial shape c by a control branch, where two branches have the same network structure without parameter sharing. Owing to the compact shape representation in 3D volume space, both complete and incomplete shapes are encoded into multi-resolution feature volumes with preserved spatial structures. Then, we hierarchically aggregate their features at each network level, as the sizes of two feature volumes are always aligned. In this work, we simply add up the two feature volumes to allow for a spatially-consistent feature aggregation, i.e., only features at the same 3D location are combined. Compared with frequently-used cross-attention technique [11, 13, 56], doing so can significantly reduce computation costs. By multi-scale feature interaction, the network can effectively correlate the difference in partialness between two shapes, both locally and globally, to learn the completion regularities. The final integrated features are then used to predict the noise volume ϵ_θ .

Network architecture. Fig. 2 provides an overview of our network architecture, which has a main branch and a control branch to respectively handle complete and incomplete shapes. The main branch (upper) is a 3D U-Net modified from a 2D version [58]. It takes as input an corrupted complete shape x_t , including (i) a pre-processing block $\varepsilon_x(\cdot)$ of two convolution layers to project x_t into a high-dimension space, (ii) N subsequent encoder blocks, denoted as $\{F_x^i(\cdot)\}_{i=1}^N$, to progressively encode and downsample the corrupted shape x_t into a collection of multi-scale features, (iii) a middle block $M_x(\cdot)$ with a self-attention layer to incorporate non-local information into the encoded feature volume, and (iv) N decoder blocks $\{D_x^i(\cdot)\}_{i=1}^N$ that sequentially upsample features through an inversion convolution to produce a feature volume of the same size as the input x_t . The term “e(d)ncoder/middle block” denotes a group of neural layers commonly adopted as a unit in neural networks, e.g., a “resnet+downsample” block.

We use a control branch (bottom) to extract the features of incomplete scan(s). Likewise, we employ a pre-processing block, N encoder blocks, and a middle block to extract multi-scale features from the conditional input, denoted as $\varepsilon_c(\cdot)$, $\{F_c^i(\cdot)\}_{i=1}^N$, and M_c , respectively. They mirror the architecture of

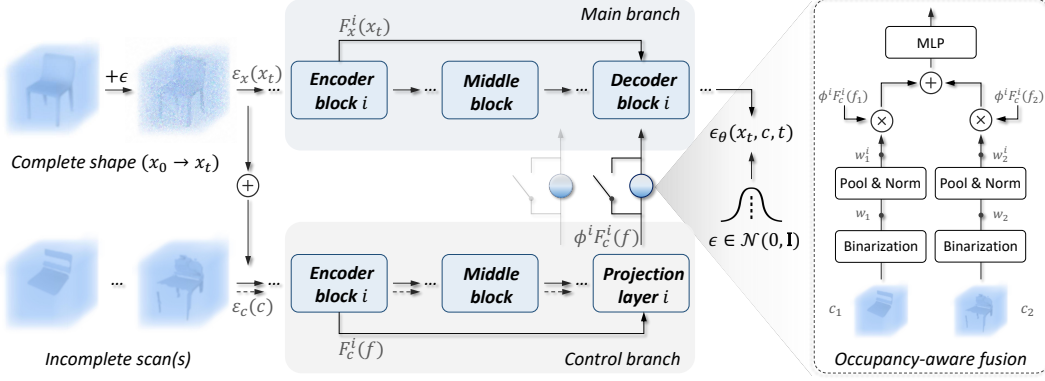


Figure 2: Given a corrupted complete shape x_t (diffused from x_0) and an incomplete scan c , we first process them into $\varepsilon_x(x_t)$ and $\varepsilon_c(c)$ to align the distributions. We employ a main branch to forward $\varepsilon_x(x_t)$, and a control branch to propagate their fused features f into deep layers. Multi-level features of f are aggregated into the main branch for hierarchical control in predicting the diffusion noise. To support multiple partial scans as condition, e.g., two scans $\{c_1, c_2\}$, we switch on occupancy-aware fusion (Sec. 3.3). This strategy utilizes the occupancy masks to enable a weighted feature fusion for c_1 and c_2 by considering their geometry reliability before feeding them into the main branch.

the corresponding blocks in the upper branch, yet operating with non-shared parameters, considering the different input data regularities (e.g., complete and sparse). Unlike the upper branch, there are no decoders for computation efficiency. Instead, we append a projection layer after each encoder/middle block F_c^i/M_c to forward multi-scale features and feed them into the decoder blocks of the main branch. As diffusion models are time-conditioned, we also convert the time step t into an embedding via two MLPs and add it to the volume features in each network block (the blue box in Fig. 2).

Hierarchical feature aggregation. To integrate the features of the complete and incomplete shapes for conditional control, we fuse them across multiple network levels. In this process, we first consider a *single* incomplete shape (denoted as c) as the condition. Given the significant disparity between c and x_t (incomplete v.s. complete, TSDF v.s. TUDF), we employ the pre-processing layers ($\varepsilon_x(\cdot)$ and $\varepsilon_c(\cdot)$) to first align their distributions before fusing them into feature volume f , i.e., $f = \varepsilon_x(x_t) + \varepsilon_c(c)$. Then, f is passed through the control branch to better propagate the useful information to the deeper layers. In turn, we use multi-scale condition features from the control branch to guide each level of decoder blocks $\{D_x^i(\cdot)\}_{i=1}^N$ in the main branch. The features that enter the i -th decoder block are denoted as

$$d^i = [D_x^{i-1}(x_t), F_x^i(x_t) + \phi^i(F_c^i(f))], \quad f = \varepsilon_x(x_t) + \varepsilon_c(c) \quad (4)$$

where $[\cdot, \cdot]$ is the concatenation operation and ϕ^i is one 1×1 convolution layer for feature projection. For simplicity, we use $F_x^i(x_0)$ to denote the features of the x_0 after the i -th encoder block $F_x^i(\cdot)$, as x_0 is not directly processed by $F_x^i(\cdot)$; the same notation is used for $F_c^i(f)$ and $D_x^{i-1}(x_t)$. The feature after the final decoder block is the network output $\epsilon_\theta(x_t, t, c)$.

By such a design, we can hierarchically incorporate conditional features, leveraging both their local and broader contexts to optimize the network outputs. Interestingly, we observe that adjusting the network level for feature aggregation can alter a trade-off between completion accuracy and diversity. Specifically, if we only aggregate features at the low-resolution network layers, we might miss finer geometry details present in the higher-resolution layers. This could reduce completion accuracy, as the model has less contextual information to work with. In contrast, if aggregating features at all levels, the effective control might make completion results closely resemble the ground truths, yet lowering the diversity. Further ablation study is provided in Sec. 4.5.

3.3 Occupancy-aware Fusion

Our framework can also take multiple incomplete scans as inputs. This option not only provides richer information to constrain the completed shape geometry but also enhances the approach’s practicality, particularly in scenarios that a single-pass scan may not fully capture the entire object. Our critical design is to effectively fuse multiple partial shape features. As averaging the original

TSDF volumes is sensitive to registration noise, we first register multiple partial shapes (*e.g.*, using Fast-Robust-ICP [69]) and propose an occupancy-aware approach to fuse them in the feature space.

Given a set of incomplete shapes of the same object, denoted as $\{c_1, \dots, c_M\}$, we individually feed them into the control branch to produce feature volumes $\{F_c^i(f_1), \dots, F_c^i(f_M)\}$ after the i -th encoder block. Before feeding them into the decoder D_x^i , we refer to their occupancy masks to perform a weighted feature average. Concretely, we first compute the original occupancy mask for each partial shape based on the TSDF values, *i.e.*, $w_j = (\text{abs}(c_j) < \tau) \in \mathbf{B}^{S \times S \times S}$ for the j -th partial shape. τ is a pre-defined threshold that assigns the volumes near the object surface as occupied and the rest as unoccupied; \mathbf{B} is a binary tensor. Then, we perform a pooling operation to resize w_j into w_j^i to align the resolution with feature volume $F_c^i(f_j)$ and normalize w_j^i by $w_j^i = w_j^i / (w_0^i + \dots + w_M^i)$. For the voxels with zero values across all occupancy masks, we uniformly assign them a 1e-2 value to avoid the division-by-zero issue. We rewrite Eq. (4), which is for single partial shape condition, as

$$d^i = [D_x^{i-1}(x_t), F_x^i(x_t) + \psi(\sum_j w_j^i \phi^i(F_c^i(f_j)))], \quad f_j = \varepsilon_x(x_t) + \varepsilon_c(c_j) \quad (5)$$

where ψ is an MLP layer to refine the fused condition features, aiming to mitigate the discrepancies among different partial shape features, as validated in Sec. 4.4. The right part of Fig. 2 illustrates the above process with two incomplete scans as the inputs.

3.4 Training and Inference

We first train the network with a single incomplete shape as the conditional input. In this phase, all the network parameters, except the MLP layer ψ for occupancy-aware fusion (in Eq. (5)), are trained with the objective in Eq. (3). When the network converges, we lock the optimized network parameters and efficiently finetune the MLP layer ψ with multiple incomplete shapes as input.

At the inference stage, we randomize a 3D noise volume as x_T from the standard Gaussian distribution. The trained completion networks are then employed for T iterations to produce x_0 from x_T conditioned on partial shape(s) c . The occupancy-aware fusion is activated only for multi-condition completion. To accelerate the inference process, we adopt a technique from [60] to sub-sample a set of time steps from $[1, \dots, T/10]$ during inference. After obtaining the generated shape volume x_0 , we extract an explicit 3D mesh using the marching cube algorithm [70].

4 Experiment

4.1 Experimental Setup

Benchmarks. We evaluate on two large-scale shape completion benchmarks: 3D-EPN [14] and PatchComplete [15]. 3D-EPN comprises 25,590 object instances of eight classes in ShapeNet [71]. For each instance, six partial scans of varying completeness are created in the 32^3 TSDF volumes by virtual scanning; the ground-truth counterpart, represented by 32^3 TUDF, is obtained by a distance field transform on a 3D scanline method [72]. While using a similar data generation pipeline, PatchComplete emphasizes completing objects of unseen categories. It includes both the synthetic data from ShapeNet [71] and the challenging real data from ScanNet [73]. For a fair comparison, we follow their data splits and evaluation metrics, *i.e.*, mean l_1 error on the TUDF predictions across all voxels on 3D-EPN, and l_1 Chamfer Distance (CD) and Intersection over Union (IoU) between the predicted and ground-truth shapes on PatchComplete. As these metrics only measure the completion accuracy, we introduce other metrics in Sec. 4.3 to compare multimodal completion characteristics.

Implementation details. We first train our network using a single partial scan as input by 200k iterations on four RTX3090 GPUs, taking around two days. If multiple conditions are needed, we finetune project layers ψ for additional 50k iterations. Adam optimizer [74] is employed with a learning rate of $1e^{-4}$ and the batch size is 32. On the 3D-EPN benchmark, we train a specific model for completing shapes of each known category; while on PatchComplete, we merge all object categories to optimize one model to promote general completion learning. Due to the unknown class IDs at test time, no classifier-guided [55] or classifier-free [75] sampling techniques are used in our diffusion model. The truncation distance in TSDF/TUDFs is set as 3 voxel units. More details about network architecture and experiments are available in the supplementary file. Unless otherwise specified, we report the results on *single* partial shape completion.

Table 1: Quantitative shape completion results on objects of known categories [14].

l_1 -err. (\downarrow)	Avg. (\downarrow)	Chair	Table	Sofa	Lamp	Plane	Car	Dresser	Boat
3D-EPN [14]	0.374	0.418	0.377	0.392	0.388	0.421	0.259	0.381	0.356
SDF-StyleGAN [51]	0.278	0.321	0.256	0.289	0.280	0.295	0.224	0.273	0.282
RePaint-3D [76]	0.266	0.289	0.264	0.266	0.268	0.302	0.214	0.285	0.243
AutoSDF [6]	0.217	0.201	0.258	0.226	0.275	0.184	0.187	0.248	0.157
PatchComplete [15]	0.088	0.134	0.095	0.084	0.087	0.061	0.053	0.134	0.058
DiffComplete (Ours)	0.053	0.070	0.073	0.061	0.059	0.015	0.025	0.086	0.031

Table 2: Shape completion results on synthetic objects [71] of unseen categories. \cdot/\cdot means CD/IoU.

CD(\downarrow)/IoU(\uparrow)	3D-EPN [14]	Few-Shot [77]	IF-Nets [49]	Auto-SDF [6]	PatchComplete [15]	Ours
Bag	5.01 / 73.8	8.00 / 56.1	4.77 / 69.8	5.81 / 56.3	3.94 / 77.6	3.86 / 78.3
Lamp	8.07 / 47.2	15.1 / 25.4	5.70 / 50.8	6.57 / 39.1	4.68 / 56.4	4.80 / 57.9
Bathtub	4.21 / 57.9	7.05 / 45.7	4.72 / 55.0	5.17 / 41.0	3.78 / 66.3	3.52 / 68.9
Bed	5.84 / 58.4	10.0 / 39.6	5.34 / 60.7	6.01 / 44.6	4.49 / 66.8	4.16 / 67.1
Basket	7.90 / 54.0	8.72 / 40.6	4.44 / 50.2	6.70 / 39.8	5.15 / 61.0	4.94 / 65.5
Printer	5.15 / 73.6	9.26 / 56.7	5.83 / 70.5	7.52 / 49.9	4.63 / 77.6	4.40 / 76.8
Laptop	3.90 / 62.0	10.4 / 31.3	6.47 / 58.3	4.81 / 51.1	3.77 / 63.8	3.52 / 67.4
Bench	4.54 / 48.3	8.11 / 27.2	5.03 / 49.7	4.31 / 39.5	3.70 / 53.9	3.56 / 58.2
Avg.	5.58 / 59.4	9.58 / 40.3	5.29 / 58.1	5.86 / 45.2	4.27 / 65.4	4.10 / 67.5

Table 3: Shape completion results on real-world objects [73] of unseen categories. \cdot/\cdot means CD/IoU.

CD(\downarrow)/IoU(\uparrow)	3D-EPN [14]	Few-Shot [77]	IF-Nets [49]	Auto-SDF [6]	PatchComplete [15]	Ours
Bag	8.83 / 53.7	9.10 / 44.9	8.96 / 44.2	9.30 / 48.7	8.23 / 58.3	7.05 / 48.5
Lamp	14.3 / 20.7	11.9 / 19.6	10.2 / 24.9	11.2 / 24.4	9.42 / 28.4	6.84 / 30.5
Bathtub	7.56 / 41.0	7.77 / 38.2	7.19 / 39.5	7.84 / 36.6	6.77 / 48.0	8.22 / 48.5
Bed	7.76 / 47.8	9.07 / 34.9	8.24 / 44.9	7.91 / 38.0	7.24 / 48.4	7.20 / 46.6
Basket	7.74 / 36.5	8.02 / 34.3	6.74 / 42.7	7.54 / 36.1	6.60 / 45.5	7.42 / 59.2
Printer	8.36 / 63.0	8.30 / 62.2	8.28 / 60.7	9.66 / 49.9	6.84 / 70.5	6.36 / 74.5
Avg.	9.09 / 44.0	9.02 / 38.6	8.26 / 42.6	8.90 / 38.9	7.52 / 49.5	7.18 / 51.3

4.2 Main Results

Completion on known object categories. On the 3D-EPN benchmark, we compare DiffComplete against SOTA deterministic [14, 15, 51] and probabilistic [6, 76] methods in terms of completion accuracy (*i.e.*, l_1 errors). For probabilistic methods, we use the average results from five inferences, each with random initialization, to account for multimodal outcomes. As shown in Table 1 and Fig. 3, DiffComplete improves over state of the arts by 40% on l_1 error (0.053 v.s. 0.088), as well as producing more realistic and high-fidelity shapes. Unlike 3D-EPN [14] and PatchComplete [15] that learn a one-step map function for shape completion, we iteratively refine the generated shape, thus significantly mitigating the surface artifacts; see comparisons of 3D-EPN and Ours in Fig. 3. Compared to GAN-based SDF-StyleGAN [51] and AutoEncoding-based AutoSDF [6], our diffusion model offers superior mode coverage and sampling quality. RePaint-3D is adapted from RePaint [76], a 2D diffusion-based inpainting method that only involves partial shape conditions during the inference process. In contrast, our DiffComplete explicitly matches each partial shape with a complete counterpart at the training stage, thereby improving the output consistency with the ground truths.

Completion on unseen object categories. In two datasets of the PatchComplete benchmark, we compare the generalizability of DiffComplete against the state of the arts, including approaches particularly designed for unseen-class completion [77, 15]. As summarized in Table 2, our method exhibits the best completion quality on average for eight unseen object categories in the synthetic ShapeNet data, despite lacking zero-shot designs. The previous SOTA PatchComplete, mainly leverages the multi-scale structural information to improve the completion robustness. Our method inherently embraces this concept within the diffusion models. With our hierarchical feature aggregation, the network learns multi-scale local completion patterns, which could generalize to various object classes, as their local structures are often shared. Our ablation study in Sec. 4.5 further validates this benefit. Table 3 demonstrates our method’s superior performance with real-world scans, which are often cluttered and noisy. As showcased in Fig. 4, the 3D shapes produced by DiffComplete stand out for their impressive global coherence and local details.



Figure 3: Shape Completion on various known object classes. We achieve the best completion quality.

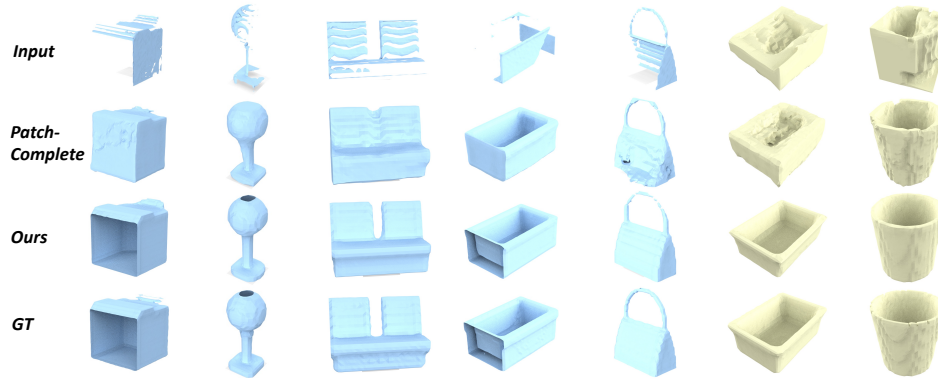


Figure 4: Shape completion on synthetic (blue) and real (yellow) objects of *entirely unseen* classes. Our method produces the completed shapes in superior quality given both synthetic and real data.

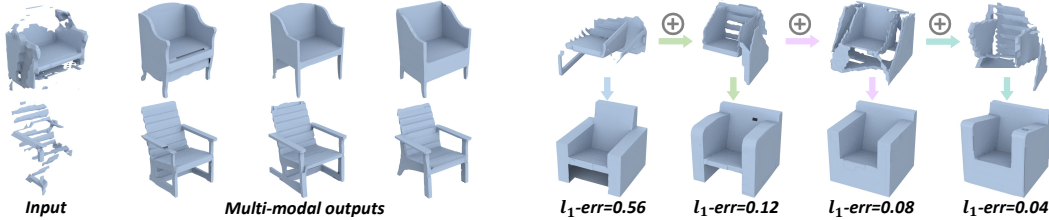


Figure 5: Our method produces multimodal plausible results given the same partial shape.

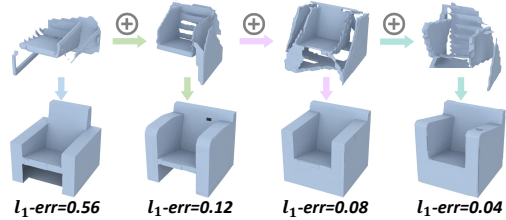


Figure 6: Our method incorporates multiple partial shapes to refine completion results (l_1 -err. \downarrow).

4.3 Multimodal Completion Characteristics

Quantitative evaluations. Probabilistic methods have the intriguing ability to produce multiple plausible completions on the same partial shape, known as multimodal completion. For the 3D-EPN chair class, we generate ten results per partial shape with randomized initial noise x_T , and employ metrics from prior works [7, 6], *i.e.*, (i) MMD measures the completion accuracy against the ground truths, (ii) TMD for completion diversity, and (iii) UHD for completion fidelity to a partial input. Table 4 shows that our method attains much better completion accuracy and fidelity, while exhibiting moderate diversity. This aligns with our design choice of leveraging the control mechanism to prioritize completion accuracy over diversity. Yet, we can adjust this trade-off to improve shape diversity, as discussed in Sec. 4.5. Fig. 5 presents our multimodal outputs, all showing great realism.

Table 4: Multimodal capacity.

Method	MMD ↓	TMD ↑	UHD ↓
AutoSDF [6]	0.008	0.028	0.061
RePaint-3D [76]	0.007	0.029	0.053
Ours	0.002	0.025	0.032

Figure 7: TMD curve.

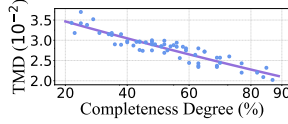


Table 5: Multi-condition results.

Cond. Num.	l_1 -err. ↓	MMD ↓	TMD ↑
one	0.07	0.002	0.025
two	0.05	0.001	0.021
three	0.04	0.001	0.019

Table 6: Effects of fusion choices for multiple conditional inputs.

Strategy	l_1 -err. ↓	CD ↓	IoU ↑
simple average	0.13	4.56	63.3
w/o MLP ψ	0.23	5.88	57.4
occ-aware (Ours)	0.05	3.97	68.3

Table 7: Feat. aggregation levels.

1/8	1/4	1/2	1	MMD ↓	TMD ↑	CD ↓
✓				0.005	0.031	4.8
✓	✓			0.004	0.028	4.4
✓	✓	✓		0.003	0.026	4.2
✓	✓	✓	✓	0.002	0.025	4.1

Table 8: Ablation on different feature aggregation manners.

Operation	l_1 -err. ↓	MMD ↓	TMD ↑
cross-attn.	0.12	0.005	0.027
concat.	0.07	0.002	0.024
addition (Ours)	0.07	0.002	0.025

Effects of input completeness degree. To verify the influence of input completeness degree on diversity, we select ten chair instances from ShapeNet, due to chair’s large structural variation. For each instance, we create six virtual scans of varying completeness, and for each scan, we generate ten diverse completions to compute their MMD. Fig. 7 presents a negative correlation between the shape diversity (reflected by MMD) and input completeness degree, which is measured by the occupied voxel’s ratio between the partial and complete GT shapes.

4.4 Multiple Conditional Inputs

Quantitative evaluations. As indicated in Table 5, DiffComplete consistently improves completion accuracy (lower l_1 error) and reduces diversity (lower TMD) when more conditional inputs are added. Fig. 1(b) and 6 showcase the progression of completion results when we gradually introduce more partial shapes of the same object (denoted by the plus symbol). Our model incorporates the local structures of all partial inputs and harmonizes them into a coherent final shape with the lower l_1 error.

Effects of occupancy-aware fusion. In Table 6, we compare our design with alternatives on the 3D-EPN chair class and PatchComplete benchmark using two conditional inputs. Averaging features without occupancy masks largely lowers the completion accuracy due to disturbances from non-informative free-space features. Removing the learnable MLP layer ψ hinders the network’s adaptation from single to multiple conditions, also worsening the results. Instead, we adaptively aggregate multi-condition features and refine them to mitigate their discrepancy for reliable completions.

4.5 Ablation Study

Effects of hierarchical feature aggregation. Table 7 shows the effects of aggregating features of the complete and incomplete shapes at different decoder levels (see Eq. (4)). First, increasing feature aggregation layers (from single to hierarchical) consistently boosts the completion accuracy (lower MMD), while decreasing it yields better diversity (higher TMD). If connecting features only at the network layer with 1/8 resolution, we achieve the best TMD that surpasses other methods (see Table 4). Thus, the accuracy-diversity trade-off can be adjusted by altering the level of feature aggregation. Second, hierarchical feature aggregation facilitates unseen-class completion (lower CD, tested on PatchComplete benchmark). This improvement suggests that leveraging multi-scale structural information from partial inputs enhances the completion robustness.

Effects of feature aggregation manner. We ablate on the way to aggregate $F_x^i(x_t)$ and $\phi^i(F_c^i(f))$ in Eq. (4). As Table 8 shows, direct addition achieves the best completion accuracy (the lowest l_1 -err and MMD), as it only combines features at the same 3D location to precisely correlate their difference for completion. Cross-attention disrupts this spatial consistency and yields less accurate results. Concatenation has a similar performance with addition, while the latter is more efficient.

5 Conclusion and Discussion

We presented DiffComplete, a new diffusion-based approach to enable multimodal, realistic, and high-fidelity 3D shape completion, surpassing prior approaches on completion accuracy and quality. This success is attributed to two key designs: a hierarchical feature aggregation mechanism for effective conditional control and an occupancy-aware fusion strategy to seamlessly incorporate

additional inputs for geometry refinement. Also, DiffComplete exhibits robust generalization to unseen object classes for both synthetic and real data, and allows an adjustable balance between completion diversity and accuracy to suit specific needs. These features position DiffComplete as a powerful tool in various applications in 3D perception and content creation. Yet, as with most diffusion models, DiffComplete requires additional computation due to its multi-step inference. A comprehensive discussion on the limitation and broader impact is provided in the supplementary file.

References

- [1] Michael Zollhöfer, Patrick Stotko, Andreas Görlitz, Christian Theobalt, Matthias Nießner, Reinhard Klein, and Andreas Kolb. State of the art on 3d reconstruction with rgb-d cameras. *Computer Graphics Forum*, 37:625–652, 05 2018. [1](#)
- [2] Angela Dai, Matthias Nießner, Michael Zollhöfer, Shahram Izadi, and Christian Theobalt. Bundlefusion: Real-time globally consistent 3d reconstruction using on-the-fly surface reintegration. *ACM Trans. Graph.*, 36(3):24:1–24:18, 2017. [1](#), [3](#)
- [3] Dejan Azinović, Ricardo Martin-Brualla, Dan B Goldman, Matthias Nießner, and Justus Thies. Neural rgb-d surface reconstruction. In *Proceedings of the IEEE/CVF Conference on Computer Vision and Pattern Recognition*, pages 6290–6301, 2022. [3](#)
- [4] Jeong Joon Park, Peter Florence, Julian Straub, Richard Newcombe, and Steven Lovegrove. DeepSDF: Learning continuous signed distance functions for shape representation. In *Proceedings of the IEEE/CVF conference on computer vision and pattern recognition*, pages 165–174, 2019.
- [5] Lior Yariv, Yoni Kasten, Dror Moran, Meirav Galun, Matan Atzmon, Basri Ronen, and Yaron Lipman. Multiview neural surface reconstruction by disentangling geometry and appearance. *Advances in Neural Information Processing Systems*, 33:2492–2502, 2020. [1](#)
- [6] Paritosh Mittal, Yen-Chi Cheng, Maneesh Singh, and Shubham Tulsiani. Autosdf: Shape priors for 3d completion, reconstruction and generation. In *Proceedings of the IEEE/CVF Conference on Computer Vision and Pattern Recognition*, pages 306–315, 2022. [2](#), [3](#), [7](#), [8](#), [9](#)
- [7] Rundi Wu, Xuelin Chen, Yixin Zhuang, and Baoquan Chen. Multimodal shape completion via conditional generative adversarial networks. In *Computer Vision—ECCV 2020: 16th European Conference, Glasgow, UK, August 23–28, 2020, Proceedings, Part IV 16*, pages 281–296. Springer, 2020. [2](#), [3](#), [8](#)
- [8] Edward J Smith and David Meger. Improved adversarial systems for 3d object generation and reconstruction. In *Conference on Robot Learning*, pages 87–96. PMLR, 2017. [3](#)
- [9] Junzhe Zhang, Xinyi Chen, Zhongang Cai, Liang Pan, Haiyu Zhao, Shuai Yi, Chai Kiat Yeo, Bo Dai, and Chen Change Loy. Unsupervised 3d shape completion through gan inversion. In *Proceedings of the IEEE/CVF Conference on Computer Vision and Pattern Recognition*, pages 1768–1777, 2021. [2](#), [3](#)
- [10] Norman Müller, Yawar Siddiqui, Lorenzo Porzi, Samuel Rota Bulò, Peter Kotschieder, and Matthias Nießner. DiffRF: Rendering-guided 3d radiance field diffusion. *arXiv preprint arXiv:2212.01206*, 2022. [2](#), [3](#), [4](#)
- [11] Yen-Chi Cheng, Hsin-Ying Lee, Sergey Tulyakov, Alexander Schwing, and Liangyan Gui. Sdfusion: Multimodal 3d shape completion, reconstruction, and generation. *arXiv preprint arXiv:2212.04493*, 2022. [3](#), [4](#)
- [12] Linqi Zhou, Yilun Du, and Jiajun Wu. 3d shape generation and completion through point-voxel diffusion. In *Proceedings of the IEEE/CVF International Conference on Computer Vision*, pages 5826–5835, 2021. [3](#)
- [13] Gene Chou, Yuval Bahat, and Felix Heide. Diffusionsdf: Conditional generative modeling of signed distance functions. *arXiv preprint arXiv:2211.13757*, 2022. [2](#), [3](#), [4](#)

- [14] Angela Dai, Charles Ruizhongtai Qi, and Matthias Nießner. Shape completion using 3d-encoder-predictor cnns and shape synthesis. In *Proceedings of the IEEE conference on computer vision and pattern recognition*, pages 5868–5877, 2017. 2, 3, 6, 7, 16
- [15] Yuchen Rao, Yinyu Nie, and Angela Dai. Patchcomplete: Learning multi-resolution patch priors for 3d shape completion on unseen categories. *arXiv preprint arXiv:2206.04916*, 2022. 2, 3, 6, 7, 16, 20, 21
- [16] Jakob Engel, Thomas Schöps, and Daniel Cremers. Lsd-slam: Large-scale direct monocular slam. In *Computer Vision–ECCV 2014: 13th European Conference, Zurich, Switzerland, September 6–12, 2014, Proceedings, Part II 13*, pages 834–849. Springer, 2014. 3
- [17] Raul Mur-Artal, Jose Maria Martinez Montiel, and Juan D Tardos. Orb-slam: a versatile and accurate monocular slam system. *IEEE transactions on robotics*, 31(5):1147–1163, 2015.
- [18] Thomas Whelan, Stefan Leutenegger, Renato F. Salas-Moreno, Ben Glocker, and Andrew J. Davison. Elasticfusion: Dense SLAM without A pose graph. In *Robotics: Science and Systems XI, Sapienza University of Rome, Rome, Italy, July 13–17, 2015*, 2015.
- [19] R. Maier, K. Kim, D. Cremers, J. Kautz, and M. Nießner. Intrinsic3d: High-quality 3D reconstruction by joint appearance and geometry optimization with spatially-varying lighting. In *International Conference on Computer Vision (ICCV)*, Venice, Italy, October 2017.
- [20] Michael Zollhöfer, Angela Dai, Matthias Innmann, Chenglei Wu, Marc Stamminger, Christian Theobalt, and Matthias Nießner. Shading-based refinement on volumetric signed distance functions. *ACM Transactions on Graphics (TOG)*, 2015. 3
- [21] Brian Curless and Marc Levoy. A volumetric method for building complex models from range images. In *Proceedings of the 23rd Annual Conference on Computer Graphics and Interactive Techniques, SIGGRAPH 1996, New Orleans, LA, USA, August 4–9, 1996*, pages 303–312, 1996. 3
- [22] Shahram Izadi, David Kim, Otmar Hilliges, David Molyneaux, Richard A. Newcombe, Pushmeet Kohli, Jamie Shotton, Steve Hodges, Dustin Freeman, Andrew J. Davison, and Andrew W. Fitzgibbon. Kinectfusion: real-time 3d reconstruction and interaction using a moving depth camera. In *Proceedings of the 24th Annual ACM Symposium on User Interface Software and Technology, Santa Barbara, CA, USA, October 16–19, 2011*, pages 559–568, 2011. 3
- [23] Richard A. Newcombe, Shahram Izadi, Otmar Hilliges, David Molyneaux, David Kim, Andrew J. Davison, Pushmeet Kohli, Jamie Shotton, Steve Hodges, and Andrew W. Fitzgibbon. Kinectfusion: Real-time dense surface mapping and tracking. In *10th IEEE International Symposium on Mixed and Augmented Reality, ISMAR 2011, Basel, Switzerland, October 26–29, 2011*, pages 127–136, 2011. 3
- [24] Matthias Nießner, Michael Zollhöfer, Shahram Izadi, and Marc Stamminger. Real-time 3d reconstruction at scale using voxel hashing. *ACM Transactions on Graphics (ToG)*, 32(6):1–11, 2013. 3
- [25] Silvan Weder, Johannes Schonberger, Marc Pollefeys, and Martin R Oswald. Routedfusion: Learning real-time depth map fusion. In *Proceedings of the IEEE/CVF Conference on Computer Vision and Pattern Recognition*, pages 4887–4897, 2020. 3
- [26] Songyou Peng, Michael Niemeyer, Lars Mescheder, Marc Pollefeys, and Andreas Geiger. Convolutional occupancy networks. In *Computer Vision–ECCV 2020: 16th European Conference, Glasgow, UK, August 23–28, 2020, Proceedings, Part III 16*, pages 523–540. Springer, 2020.
- [27] Ang Li, Zejian Yuan, Yonggen Ling, Wanchao Chi, Chong Zhang, et al. A multi-scale guided cascade hourglass network for depth completion. In *Proceedings of the IEEE/CVF Winter Conference on Applications of Computer Vision*, pages 32–40, 2020.
- [28] Angela Dai, Yawar Siddiqui, Justus Thies, Julien Valentin, and Matthias Nießner. Spsg: Self-supervised photometric scene generation from rgb-d scans. In *Proceedings of the IEEE/CVF Conference on Computer Vision and Pattern Recognition*, pages 1747–1756, 2021. 3

- [29] Olga Sorkine and Daniel Cohen-Or. Least-squares meshes. In *Proceedings Shape Modeling Applications, 2004.*, pages 191–199. IEEE, 2004. 3
- [30] Andrew Nealen, Takeo Igarashi, Olga Sorkine, and Marc Alexa. Laplacian mesh optimization. In *Proceedings of the 4th international conference on Computer graphics and interactive techniques in Australasia and Southeast Asia*, pages 381–389, 2006.
- [31] Wei Zhao, Shuming Gao, and Hongwei Lin. A robust hole-filling algorithm for triangular mesh. *The Visual Computer*, 23:987–997, 2007. 3
- [32] Michael M. Kazhdan, Matthew Bolitho, and Hugues Hoppe. Poisson surface reconstruction. In *Proceedings of the Fourth Eurographics Symposium on Geometry Processing, Cagliari, Sardinia, Italy, June 26-28, 2006*, pages 61–70, 2006. 3
- [33] Michael Kazhdan and Hugues Hoppe. Screened poisson surface reconstruction. *ACM Transactions on Graphics (ToG)*, 32(3):1–13, 2013. 3
- [34] Sebastian Thrun and Ben Wegbreit. Shape from symmetry. In *Tenth IEEE International Conference on Computer Vision (ICCV’05) Volume 1*, volume 2, pages 1824–1831. IEEE, 2005. 3
- [35] Niloy J Mitra, Leonidas J Guibas, and Mark Pauly. Partial and approximate symmetry detection for 3d geometry. *ACM Transactions on Graphics (ToG)*, 25(3):560–568, 2006.
- [36] Mark Pauly, Niloy J Mitra, Johannes Wallner, Helmut Pottmann, and Leonidas J Guibas. Discovering structural regularity in 3d geometry. In *ACM SIGGRAPH 2008 papers*. 2008.
- [37] Ivan Sipiran, Robert Gregor, and Tobias Schreck. Approximate symmetry detection in partial 3d meshes. In *Computer Graphics Forum*, 2014.
- [38] Pablo Speciale, Martin R Oswald, Andrea Cohen, and Marc Pollefeys. A symmetry prior for convex variational 3d reconstruction. In *Computer Vision–ECCV 2016: 14th European Conference, Amsterdam, The Netherlands, October 11-14, 2016, Proceedings, Part VIII 14*, pages 313–328. Springer, 2016. 3
- [39] Minhyuk Sung, Vladimir G Kim, Roland Angst, and Leonidas Guibas. Data-driven structural priors for shape completion. *ACM Transactions on Graphics (TOG)*, 34(6):1–11, 2015. 3
- [40] Yangyan Li, Angela Dai, Leonidas Guibas, and Matthias Nießner. Database-assisted object retrieval for real-time 3d reconstruction. In *Computer graphics forum*, 2015.
- [41] Liangliang Nan, Ke Xie, and Andrei Sharf. A search-classify approach for cluttered indoor scene understanding. *ACM Transactions on Graphics (TOG)*, 31(6):1–10, 2012.
- [42] Young Min Kim, Niloy J Mitra, Dong-Ming Yan, and Leonidas Guibas. Acquiring 3d indoor environments with variability and repetition. *ACM Transactions on Graphics (TOG)*, 31(6):1–11, 2012. 3
- [43] Duc Thanh Nguyen, Binh-Son Hua, Khoi Tran, Quang-Hieu Pham, and Sai-Kit Yeung. A field model for repairing 3d shapes. In *Proceedings of the IEEE Conference on Computer Vision and Pattern Recognition*, pages 5676–5684, 2016. 3
- [44] Michael Firman, Oisín Mac Aodha, Simon Julier, and Gabriel J Brostow. Structured prediction of unobserved voxels from a single depth image. In *Proceedings of the IEEE Conference on Computer Vision and Pattern Recognition*, pages 5431–5440, 2016. 3
- [45] Angela Dai, Christian Diller, and Matthias Nießner. Sg-nn: Sparse generative neural networks for self-supervised scene completion of rgb-d scans. In *Proceedings of the IEEE/CVF Conference on Computer Vision and Pattern Recognition*, pages 849–858, 2020. 3
- [46] Xumin Yu, Yongming Rao, Ziyi Wang, Zuyan Liu, Jiwen Lu, and Jie Zhou. Pointr: Diverse point cloud completion with geometry-aware transformers. In *Proceedings of the IEEE/CVF international conference on computer vision*, pages 12498–12507, 2021.

- [47] Xiaoguang Han, Zhen Li, Haibin Huang, Evangelos Kalogerakis, and Yizhou Yu. High-resolution shape completion using deep neural networks for global structure and local geometry inference. In *Proceedings of the IEEE international conference on computer vision*, pages 85–93, 2017.
- [48] Shuran Song, Fisher Yu, Andy Zeng, Angel X Chang, Manolis Savva, and Thomas Funkhouser. Semantic scene completion from a single depth image. In *Proceedings of the IEEE conference on computer vision and pattern recognition*, pages 1746–1754, 2017.
- [49] Julian Chibane, Thiemo Alldieck, and Gerard Pons-Moll. Implicit functions in feature space for 3d shape reconstruction and completion. In *Proceedings of the IEEE/CVF conference on computer vision and pattern recognition*, pages 6970–6981, 2020. 3, 7
- [50] Angela Dai and Matthias Nießner. Scan2mesh: From unstructured range scans to 3d meshes. In *Proceedings of the IEEE/CVF Conference on Computer Vision and Pattern Recognition*, pages 5574–5583, 2019. 3
- [51] X Zheng, Yang Liu, P Wang, and Xin Tong. Sdf-stylegan: Implicit sdf-based stylegan for 3d shape generation. In *Computer Graphics Forum*, 2022. 3, 7
- [52] Xuelin Chen, Baoquan Chen, and Niloy J Mitra. Unpaired point cloud completion on real scans using adversarial training. *arXiv preprint arXiv:1904.00069*, 2019. 3
- [53] Panos Achlioptas, Olga Diamanti, Ioannis Mitliagkas, and Leonidas Guibas. Learning representations and generative models for 3d point clouds. In *International conference on machine learning*, pages 40–49. PMLR, 2018. 3
- [54] Jascha Sohl-Dickstein, Eric Weiss, Niru Maheswaranathan, and Surya Ganguli. Deep unsupervised learning using nonequilibrium thermodynamics. In *International Conference on Machine Learning*, pages 2256–2265. PMLR, 2015. 3
- [55] Prafulla Dhariwal and Alexander Nichol. Diffusion models beat gans on image synthesis. *Advances in Neural Information Processing Systems*, 34:8780–8794, 2021. 6
- [56] Robin Rombach, Andreas Blattmann, Dominik Lorenz, Patrick Esser, and Björn Ommer. High-resolution image synthesis with latent diffusion models. In *Proceedings of the IEEE/CVF Conference on Computer Vision and Pattern Recognition*, pages 10684–10695, 2022. 4
- [57] Yang Song, Jascha Sohl-Dickstein, Diederik P Kingma, Abhishek Kumar, Stefano Ermon, and Ben Poole. Score-based generative modeling through stochastic differential equations. *ICLR*, 2021.
- [58] Alexander Quinn Nichol and Prafulla Dhariwal. Improved denoising diffusion probabilistic models. In *International Conference on Machine Learning*, pages 8162–8171. PMLR, 2021. 4, 18
- [59] Jonathan Ho, Ajay Jain, and Pieter Abbeel. Denoising diffusion probabilistic models. *Advances in Neural Information Processing Systems*, 33:6840–6851, 2020. 4, 18
- [60] Jiaming Song, Chenlin Meng, and Stefano Ermon. Denoising diffusion implicit models. *arXiv preprint arXiv:2010.02502*, 2020. 6, 18
- [61] Abhishek Sinha, Jiaming Song, Chenlin Meng, and Stefano Ermon. D2c: Diffusion-decoding models for few-shot conditional generation. *Advances in Neural Information Processing Systems*, 34:12533–12548, 2021. 3
- [62] Xiaohui Zeng, Arash Vahdat, Francis Williams, Zan Gojcic, Or Litany, Sanja Fidler, and Karsten Kreis. Lion: Latent point diffusion models for 3d shape generation. *arXiv preprint arXiv:2210.06978*, 2022. 3
- [63] Shitong Luo and Wei Hu. Diffusion probabilistic models for 3d point cloud generation. In *Proceedings of the IEEE/CVF Conference on Computer Vision and Pattern Recognition*, pages 2837–2845, 2021.

- [64] Alex Nichol, Heewoo Jun, Prafulla Dhariwal, Pamela Mishkin, and Mark Chen. Point-e: A system for generating 3d point clouds from complex prompts. *arXiv preprint arXiv:2212.08751*, 2022. 3
- [65] Gimin Nam, Mariem Khelifi, Andrew Rodriguez, Alberto Tono, Linqi Zhou, and Paul Guerrero. 3d-ldm: Neural implicit 3d shape generation with latent diffusion models. *arXiv preprint arXiv:2212.00842*, 2022. 3, 4
- [66] Biao Zhang, Jiapeng Tang, Matthias Niessner, and Peter Wonka. 3dshape2vecset: A 3d shape representation for neural fields and generative diffusion models. *arXiv preprint arXiv:2301.11445*, 2023. 3
- [67] Miguel Angel Bautista, Pengsheng Guo, Samira Abnar, Walter Talbott, Alexander Toshev, Zhuoyuan Chen, Laurent Dinh, Shuangfei Zhai, Hanlin Goh, Daniel Ulbricht, et al. Gaudi: A neural architect for immersive 3d scene generation. *Advances in Neural Information Processing Systems*, 35:25102–25116, 2022. 3
- [68] Lvmin Zhang and Maneesh Agrawala. Adding conditional control to text-to-image diffusion models. *arXiv preprint arXiv:2302.05543*, 2023. 4, 16
- [69] Juyong Zhang, Yuxin Yao, and Bailin Deng. Fast and robust iterative closest point. *IEEE Transactions on Pattern Analysis and Machine Intelligence*, 2021. 6
- [70] William E Lorensen and Harvey E Cline. Marching cubes: A high resolution 3d surface construction algorithm. *ACM siggraph computer graphics*, 21(4):163–169, 1987. 6
- [71] Angel X Chang, Thomas Funkhouser, Leonidas Guibas, Pat Hanrahan, Qixing Huang, Zimo Li, Silvio Savarese, Manolis Savva, Shuran Song, Hao Su, et al. Shapenet: An information-rich 3d model repository. *arXiv preprint arXiv:1512.03012*, 2015. 6, 7, 17
- [72] John Amanatides, Andrew Woo, et al. A fast voxel traversal algorithm for ray tracing. In *Eurographics*, 1987. 6
- [73] Angela Dai, Angel X Chang, Manolis Savva, Maciej Halber, Thomas Funkhouser, and Matthias Nießner. Scannet: Richly-annotated 3d reconstructions of indoor scenes. In *Proceedings of the IEEE conference on computer vision and pattern recognition*, pages 5828–5839, 2017. 6, 7
- [74] Diederik P Kingma and Jimmy Ba. Adam: A method for stochastic optimization. *arXiv preprint arXiv:1412.6980*, 2014. 6
- [75] Jonathan Ho and Tim Salimans. Classifier-free diffusion guidance. *arXiv preprint arXiv:2207.12598*, 2022. 6
- [76] Andreas Lugmayr, Martin Danelljan, Andres Romero, Fisher Yu, Radu Timofte, and Luc Van Gool. Repaint: Inpainting using denoising diffusion probabilistic models. In *Proceedings of the IEEE/CVF Conference on Computer Vision and Pattern Recognition*, pages 11461–11471, 2022. 7, 9
- [77] Bram Wallace and Bharath Hariharan. Few-shot generalization for single-image 3d reconstruction via priors. In *Proceedings of the IEEE/CVF International Conference on Computer Vision*, pages 3818–3827, 2019. 7
- [78] Hongkai Zheng, Weili Nie, Arash Vahdat, Kamyar Azizzadenesheli, and Anima Anandkumar. Fast sampling of diffusion models via operator learning. *arXiv preprint arXiv:2211.13449*, 2022. 18
- [79] Benjamin Graham, Martin Engelcke, and Laurens van der Maaten. 3d semantic segmentation with submanifold sparse convolutional networks. *CVPR*, 2018. 19
- [80] Peng-Shuai Wang, Yang Liu, Yu-Xiao Guo, Chun-Yu Sun, and Xin Tong. O-cnn: Octree-based convolutional neural networks for 3d shape analysis. *ACM Transactions On Graphics (TOG)*, 36(4):1–11, 2017. 19

Supplementary Material

Contents

A Detailed Network Architecture	15
B Additional Experiments	16
B.1 Choice of Training Strategy	16
B.2 Choice of Fusion Space for Multiple Conditions	16
B.3 Choice of Occupancy Threshold	16
B.4 Impact of Training Iteration	17
B.5 Data-efficient Finetuning on Unseen Categories	17
B.6 Failure Cases	17
C Quantitative Visualizations	18
D Limitations and Potential Solutions	18
E Broader Impact	19

A Detailed Network Architecture

Fig. 8 shows the detailed architecture of encoder blocks, middle blocks, and decoder blocks of our network (corresponding to those in Fig. 2). In particular, both the main and control branches consist of four encoder blocks (Fig. 8(a)), built from repeated ResBlocks and Downsample layers, where the latter iteratively reduces the feature volume to 1/8th of its original size. The middle block (Fig. 8(b)) comprises two ResBlocks with an intermediate AttentionBlock. The main branch additionally contains four decoder blocks (Fig. 8(c)), which restore the volume shape to its initial size using upsampling. Fig. 8(d) presents the detailed structure of a ResBlock unit. It receives features from the preceding network layer and a time embedding as inputs, fuses their embeddings, and processes them with convolutional operations. To support network and experiment reproduction, we will make our code available.

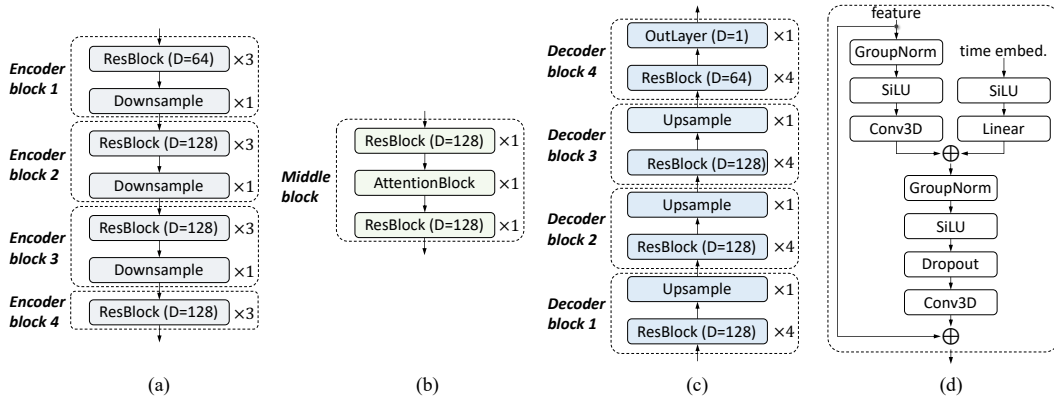


Figure 8: The detailed architecture of encoder blocks (a), middle blocks (b), and decoder blocks (c) in our network, each is mainly constructed by stacked ResBlocks (d). The ‘D’ denotes the output feature dimension and \oplus represents the feature addition operation.

Table 9: Choice of training strategy. The pretraining-based options increase the completion errors (l_1 -err.) and diversity (TMD).

Training Strategy	l_1 -err. ↓	TMD ↑
pretraining-class	0.14	0.028
pretraining-all	0.11	0.030
scratch (Ours)	0.07	0.025

Table 10: Choice of fusion space for multiple partial shapes. Directly fusing them in the original TSDF space significantly impairs the completion quality.

Space	Strategy	l_1 -err. ↓	CD ↓	IoU ↑
TSDF	simple average	0.29	6.68	51.6
	occ-aware	0.12	4.78	61.0
feature	simple average	0.13	4.56	63.3
	occ-aware	0.05	3.97	68.3

B Additional Experiments

B.1 Choice of Training Strategy

In Table 9, we evaluate different training strategies for our model on chair class of the 3D-EPN [14] benchmark. Both ‘pretraining-class’ and ‘pretraining-all’ follow ControlNet [68]’s training paradigm. They involve an initial unconditional generation task for main branch pretraining and then optimize only the control branch with partial shapes with the objective in Eq. (3). Specifically, ‘pretraining-class’ pretrains the main branch on individual object classes, while ‘pretraining-all’ employs all data for one pretraining model, both of which are finetuned on a specific object class. These pretraining-based strategies bring much more completion errors (higher l_1 -err.) and increased completion diversity (higher TMD). This may be due to the model’s over-reliance on the learned distribution during pretraining, making it less adaptable to concrete completion tasks. Instead, we train the network entirely from scratch, which is most effective for accurate shape completion (with the lowest l_1 -err.).

B.2 Choice of Fusion Space for Multiple Conditions

Table 10 analyzes the impacts of fusion space when incorporating multiple incomplete shapes as conditions, which supplements Table 6 to further validate our fusion choice. The experiments are conducted on the 3D-EPN [14] and Patchcomplete [15] benchmarks. The first two rows refer to merging multiple aligned partial shapes into a volumetric TSDF and feeding it to the network as a single condition. However, both ‘simple average’ and ‘occupancy-aware’ fusion strategies for this yield worse performance across diverse metrics. This is because registration errors between different shapes directly disrupt the input, potentially causing distortions in the final completed model. In contrast, we move the fusion process to a more abstract level within the hierarchical feature space, which can be more resilient to simple noise at the TSDF level. Our occupancy-aware fusion strategy further provides more accurate and robust completion results.

B.3 Choice of Occupancy Threshold

During the occupancy-aware fusion process, the TSDF value threshold τ determines which volumes are recognized as occupied. In Table 11, we evaluate the impact of different thresholds on the completion performance using the 3D-EPN [14] and Patchcomplete [15] benchmarks. Selecting extreme threshold values, whether very low (*e.g.*, 1 voxel unit) or high (*e.g.*, 5 voxel units), tends to degrade results, as lower thresholds may omit informative geometries while higher ones could include redundant geometries that do not contribute meaningfully to the object shape, both of which confuse the model. Conversely, a middle-range value (3 voxel unit) provides a balance between preserving essential geometries and avoiding unnecessary ones, thereby achieving optimal completion accuracy (the lowest l_1 -err. and CD).

Table 11: Choice of occupancy threshold. Extremely low or high values yield worse results.

Threshold τ	l_1 -err. \downarrow	CD \downarrow	IoU \uparrow
1	0.08	4.21	66.6
2	0.05	4.09	68.2
3 (Ours)	0.05	3.97	68.3
4	0.06	4.10	68.4
5	0.07	4.13	67.8

Figure 9: Accuracy (MMD) and diversity (TMD) curves with varying training iterations.

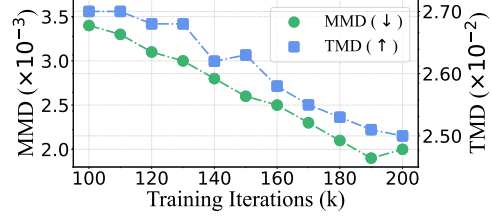


Table 12: Finetuning on eight unseen object categories with limited data. Our model shows substantial improvements with incremental data. The 0% and 100% indicate zero and full data usage, respectively.

Data Ratio	Avg. CD \downarrow	Bag	Lamp	Bathtub	Bed	Basket	Printer	Laptop	Bench
0%	3.19	2.98	3.54	2.87	3.24	3.70	3.46	2.85	2.87
1%	2.84	2.54	3.27	2.46	2.98	3.24	3.25	2.49	2.52
5%	1.84	1.67	1.93	1.63	2.01	1.96	2.04	1.81	1.70
10%	1.34	1.23	1.43	1.20	1.40	1.49	1.48	1.28	1.19
100%	1.02	0.98	1.07	0.95	1.05	1.12	1.10	1.00	0.95

B.4 Impact of Training Iteration

Fig. 9 plots the performance of our model over a range of training iterations from 100k to 200k. As the training iterations increase, the shape completion accuracy improves (with lower MMD) while the completion diversity gradually decreases (with lower TMD). This trend reveals that, given more training time, the model learns to better fit the target distribution.

B.5 Data-efficient Finetuning on Unseen Categories

In Table 12, we evaluate the model’s ability to complete ShapeNet objects [71] of unknown categories when finetuned with limited data. To this end, we first divide the data from unseen classes into a 7:3 train-test split. Then we finetune our model using varying proportions of the training set (1%, 5%, and 10%). Here, a ratio of 0% indicates no finetuning process, following the setting in Table 2, while 100% means using the entire training set. A lower CD denotes better completion accuracy.

With just 1% finetuning data, the average CD decreases by 10.9% (from 3.19 to 2.84). A more substantial improvement is observed when the data ratio increases to 5%, with a nearly 1 point decrease in average CD compared to the 1% ratio. The trend of improvement continues for a 10% data ratio, where the model impressively approaches the performance achieved using the full training set. These results demonstrate that our model has a robust few-shot learning capability and can generalize well from a small amount of out-of-distribution data.

B.6 Failure Cases

Fig. 10 showcases certain failure instances in our completion results. For shape completion on known object categories (a-c), given the overly sparse input, our model struggles with producing a shape that aligns with the ground truth (see (a) and (b)). In example (c), the model fails to complete a non-standard structure, such as an elephant beneath a lamp. This can be attributed to the model’s tendency to generate shapes based on frequently seen patterns during training, while the elephant belongs to an atypical structure in lamp categories. For unknown object categories (d-f), the model faces additional challenges. The case (d) reveals that our model may favor simple structures when the input shape is too complex. Cases (e) and (f) further show the model’s difficulty in handling substantial input noise, which results in inaccurate or improbable completions.

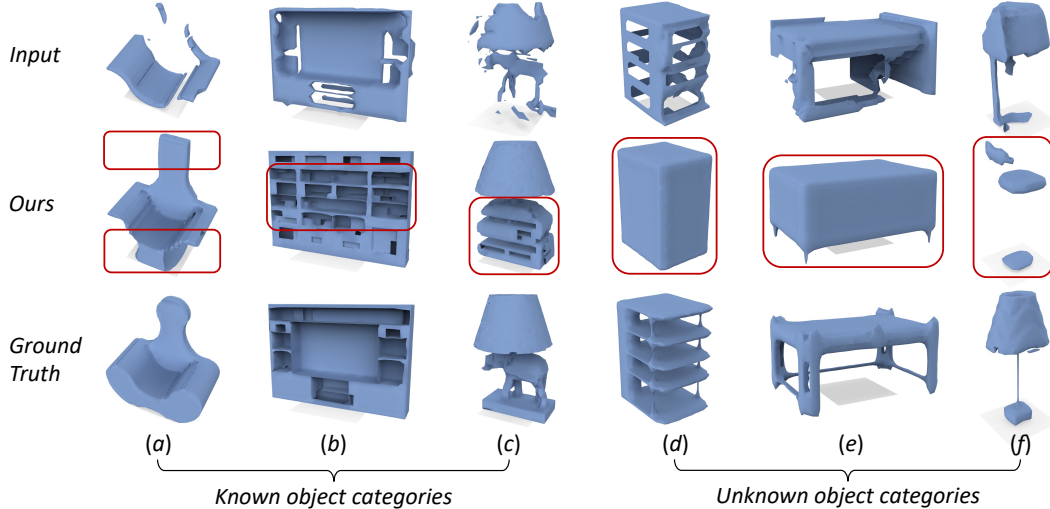


Figure 10: Failure cases on known and unknown object categories. Our model may produce inaccurate or improbable completions when faced with overly sparse inputs (a), atypical shapes (b-c), complex structures (d), and high noise levels (e-f). The red boxes highlight the difference with ground truths.

C Quantitative Visualizations

Visualizations on known object categories. Fig. 11 shows quantitative results on diverse object categories produced by SOTA PatchComplete and our DiffComplete. Our method produces the completion results with much fewer artifacts and more realistic shapes. Our completions are also highly accurate, closely recovering the ground-truth shapes.

Visualizations on unseen object categories. As shown in Fig. 12, across a diverse set of entirely unseen object categories, our method also achieves superior completion results over PatchComplete, preserving better global coherence and local details. Note that we do not employ any zero-shot designs while PatchComplete does.

Multimodal completion results. In Fig. 13, we show multiple plausible completion results produced by our model from the same partial shape input. For sparser input shapes, our model can explore different possibilities to fill in the missing regions and yield more diverse results (*e.g.*, the first row). In contrast, for the inputs with higher completeness levels, our control-based design ensures the model to output more consistent 3D shapes (*e.g.*, the last row).

Visualizations of denoising process. In Fig. 14, we visualize the produced shapes at different time steps during the inference stage. Our model progressively converts the noises into clean 3D shapes.

D Limitations and Potential Solutions

First, our model may struggle to complete highly irregular or noisy shapes, as extensively discussed in Sec. B.6. Yet, our model’s multimodal capacity will increase the likelihood of producing satisfactory results, enabling it to tackle this problem more effectively than deterministic methods. With more diverse training data, the model’s performance on completing these hard shapes could be improved.

Like most diffusion models [59, 58], another limitation of DiffComplete is the substantial computational requirements due to the iterative completion process. Despite employing the technique in work [60] to reduce sampling steps by ten times, we still need 100 steps to achieve competitive results, which costs around 3-4 seconds per shape on an RTX 3090 GPU. The extended test time could cap its potential for real-time or resource-constrained applications. Future work will leverage the advances in fast sampling techniques (*e.g.*, [78]) to accelerate inference speed.

Also, the dense 3D CNN architecture in our implementation limits the model ability to handle high-resolution 3D shapes, due to the cubic increase in computational costs with volume size. A potential

solution could be replacing dense CNNs with efficient 3D network modules, such as SparseConv [79] or Octree-based layers [80], while remaining other essential designs of our framework.

At last, although our model shows robust generalizability to unseen object classes, its performance may be adversely affected by the quality and diversity of the training data. In cases where object classes or shapes deviate significantly from the training set, the model may underperform. Therefore, careful selection of training data is needed to boost completion robustness.

In conclusion, despite the current limitations, they also present opportunities for model improvement. By addressing these issues, we believe the full potential of our model can be further realized.

E Broader Impact

On the positive side, the potential applications of our work are widespread. DiffComplete could contribute to fields such as computer vision, robotics, virtual reality, and many others. For instance, in computer vision and robotics, our method can significantly enhance object reconstruction capabilities, providing more accurate and realistic models that facilitate object recognition, manipulation, and robot navigation. Similarly, in virtual reality or 3D printing, our model is able to complete or refine 3D models, enriching the user experience and the quality of end products.

Moreover, our model provides a flexible balance between the completion diversity and accuracy. This attribute can be tailored to suit various application needs, thereby broadening its potential usability across different tasks.

On the other hand, it is crucial to consider potential negative implications. As with any AI technology, there are risks associated with misuse. For instance, if used for recreating personal items without consent, it could lead to unwarranted privacy intrusions. In addition, the automation facilitated by our model may also displace jobs involving manual 3D modeling or shape completion.

To conclude, while our research holds promising potential, it is essential to responsibly manage its broader impacts. We advocate for developing this technology in a way that maximizes societal benefits and minimizes potential negative effects.

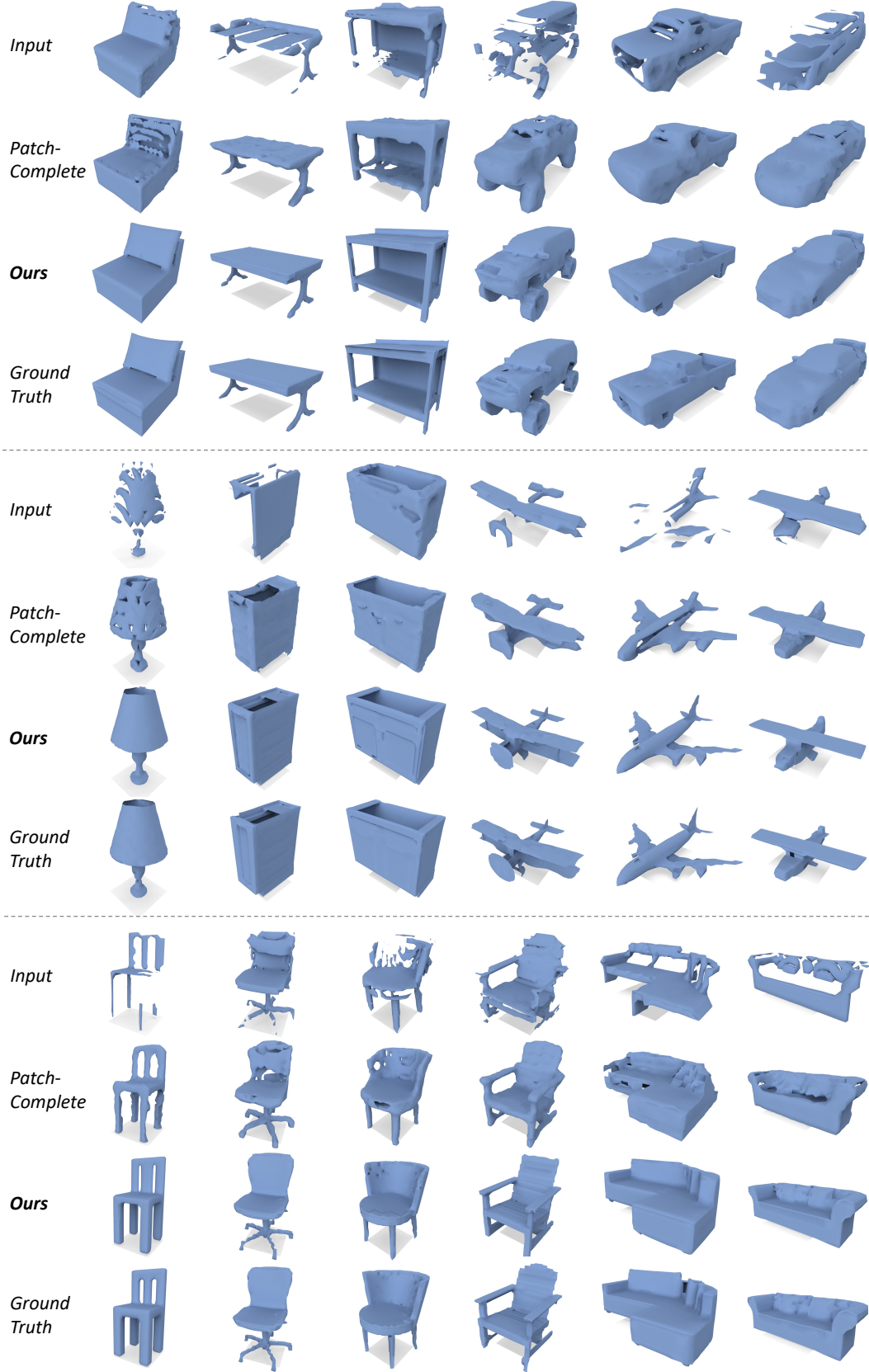


Figure 11: Quantitative results on completing objects of diverse known categories. Our method significantly outperforms SOTA PatchComplete [15] on both the completion quality and accuracy.

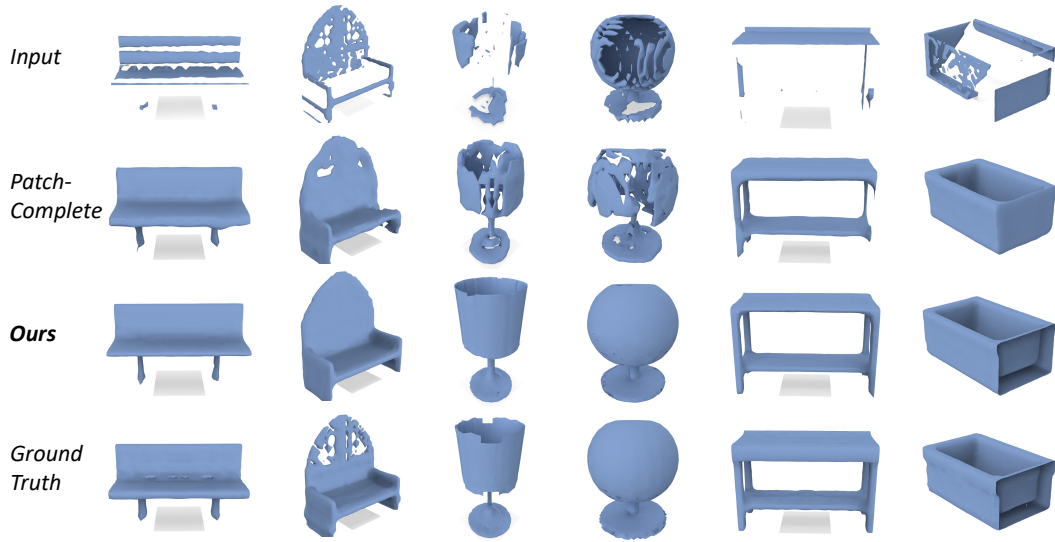


Figure 12: Quantitative results on completing objects of entirely unseen categories. Our significantly outperforms SOTA PatchComplete [15] on both the completion quality and accuracy.

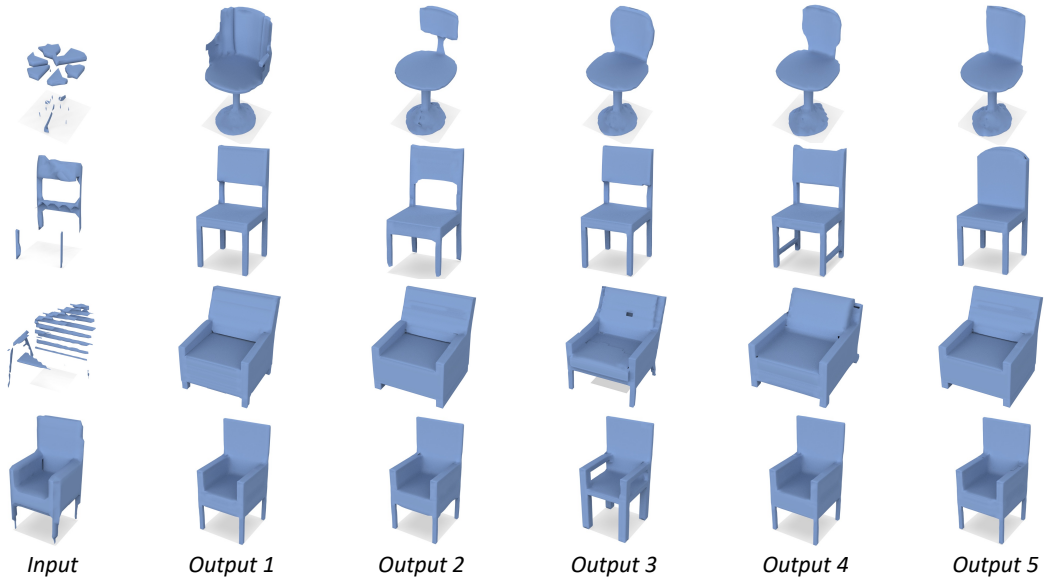


Figure 13: Multimodal completion results on ShapeNet Chair class. We run the model five times for the same input. The level of input sparsity affects the diversity and certainty of the shape completion.

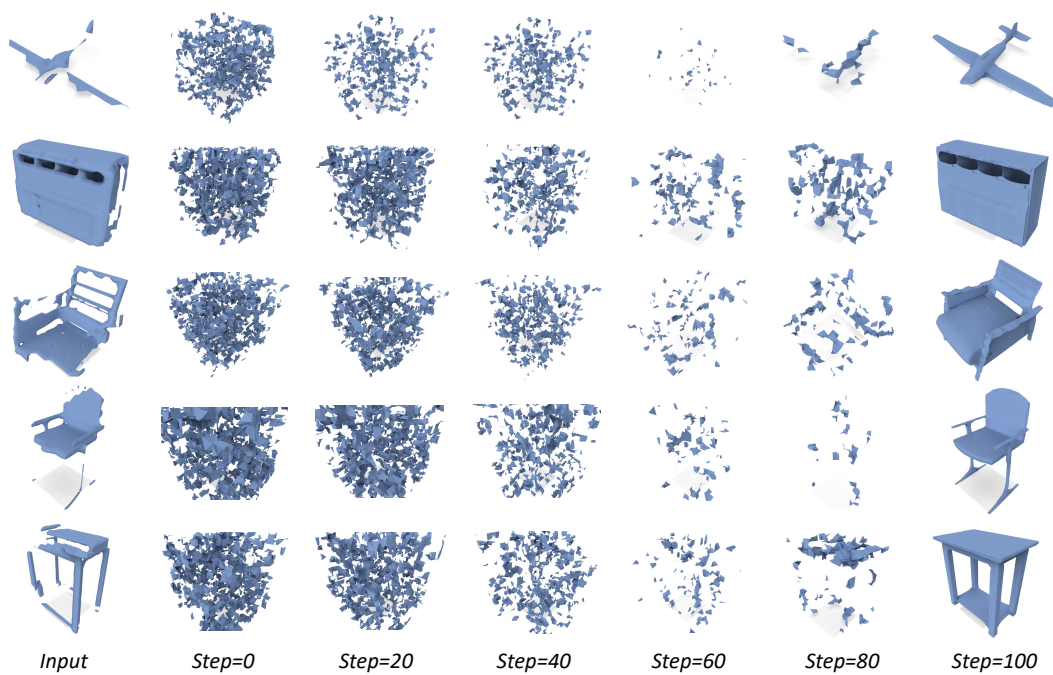


Figure 14: The denoising process that gradually converts the noises to completed shapes (from left to right). We visualize the produced shapes at varying time steps (0, 20, 40, 60, 80, and 100).